Food Chemistry 320 (2020) 126666

Contents lists available at ScienceDirect

Food Chemistry

journal homepage: www.elsevier.com/locate/foodchem

Graphene-like BN@SiO_2 nanocomposites as efficient sorbents for solid-phase extraction of Rhodamine B and Rhodamine 6G from food samples

Yanhong Chao[a], Jingyu Pang[b,c,*], Yan Bai[b,*], Peiwen Wu[c], Jing Luo[c], Jing He[c], Yan Jin[a], Xiaowei Li[c], Jun Xiong[c], Huaming Li[c], Wenshuai Zhu[c,*]

[a] School of Pharmacy, Jiangsu University, Zhenjiang 212013, PR China
[b] Key Laboratory of Polyoxometalate Chemistry of Henan Province, Institute of Molecular and Crystal Engineering, Henan University, Kaifeng 475004, PR China
[c] School of Chemistry and Chemical Engineering, Jiangsu University, Zhenjiang 212013, PR China

ARTICLE INFO

Keywords:
Boron nitride
Silica
Adsorption
Solid-phase extraction
Dye
HPLC

ABSTRACT

A novel dendritic silicon dioxide nanocomposite coated with a highly dispersed graphene-like boron nitride nanosheet (*g*-BN(x)@SiO_2) was *in-situ* synthesized and employed as a solid-phase extraction material for the Rhodamine B (RhB) and Rhodamine 6G (R6G) enrichment in food samples prior to their quantitation by HPLC. The structures and morphologies of *g*-BN(x)@SiO_2 were characterized by XRD, FTIR, BET and TEM. The adsorption performance and mechanism were investigated and showed an enhanced maximum adsorption capacity of 625 mg/g for RhB on the nanocomposite loaded with 1% of *g*-BN via a fast, spontaneous process. Under optimal extraction conditions, this method showed low detection and quantification limits (2.8 μg/L for RhB, 2.1 μg/L for R6G and 9.2 μg/L for RhB, 6.9 μg/L for R6G, respectively), good repeatability (RSD% < 3.7%), and satisfactory spiked recoveries of 94.8%–103.1% for RhB and R6G in real chili powder and beverage. Therefore, the *g*-BN(1%)@SiO_2-based materials possess significant potential.

1. Introduction

Synthetic dyes, a class of illegal additives in foodstuffs, have been considered as a serious threat to public health (He, Zhang, Hu, Bai, & Wei, 2019). Rhodamine B (RhB) and Rhodamine 6G (R6G), derivatives of xanthene dyes, have been widely employed in fluorescent labeling, textile, paper, and printing industries, due to their intense pink color (Chen & Zhu, 2016; Zhuang et al., 2019). However, they are both generally toxic and harmful to human beings and animals. They can trigger allergy and asthmatic reactions and cause irritation to the skin and the respiratory tract (Dil, Ghaedi, Asfaram, Mehrabi, & Bazrafshan, 2018).

Hence, the use of RhB and R6G in foodstuffs is strictly banned. However, owning to their low cost and color fastness, these dyes are often added illegally to food matrices as colorants to enhance visual aesthetics and promote sales. Thus, developing a simple and sensitive method for the determination of trace RhB and R6G in food samples is an urgent need. Due to the complexity of the sample matrix and the low concentration of the dyes, the direct detection by spectrophotometry or chromatography is difficult. Therefore, the extraction and enrichment of trace dyes in the matrix prior to analysis has received increased attention.

In the last decades, solid-phase extraction (SPE), as a sampling preparation technique, has been considered as a promising alternative to the classical liquid extraction method (Li, Raza, Wang, Xu, & Chen, 2017; Yan & Wang, 2015) and has been applied worldwide in environmental and food analysis. It has gained rapid acceptance due to its advantages such as the easy, fast, and solvent-free operation, the low disposal costs, the lower cross-contamination risks, and the possibility of automation (Akkaya, Erulas, Buyukpinar, & Bakirdere, 2019; Wang et al., 2019). Various column packing materials, including γ-Fe_2O_3 immobilized with imino-pyridine (Khani, Sobhani, & Yari, 2019), magnetic molecularly imprinted polymers (Bagheri et al., 2019), sodium dodecyl sulfate coated nano-magnet Fe_3O_4 (Qi et al., 2016) and others have been developed and applied in SPE to extract and preconcentration of RhB in real samples. These studies indicated that nanomaterials possessed high affinity and adsorption capacity to RhB due to their large surface areas and variety of reactive sites. Thus, the development of novel packing materials with high efficiency, low cost, easy synthesis, and high stability still remains a great challenge.

White graphitic-hexagonal boron nitride (*g*-BN) has drawn extensive attention due to its unique properties of high thermal stability, resistance to oxidation, high specific surface area, and low density (Chao et al., 2014; Wu et al., 2016). As an environmentally friendly two-

* Corresponding authors.
E-mail addresses: pjy@henu.edu.cn (J. Pang), baiyan@henu.edu.cn (Y. Bai), zhuws@ujs.edu.cn (W. Zhu).

https://doi.org/10.1016/j.foodchem.2020.126666
Received 19 September 2019; Received in revised form 19 March 2020; Accepted 20 March 2020
Available online 21 March 2020

dimensional material, *g*-BN has demonstrated attractive affinity and adsorption capacity to various organic compounds and has been used as a promising adsorbent in analytical chemistry, wastewater treatment, catalysis, and drug delivery. For example, *g*-BN synthesized via microwave heating showed high removal ability to dyes (Shen, Liu, Yan, & Wang, 2019). Boron nitride bundles could selectively adsorb antibiotic contaminants (Song et al., 2019). Fast separation of RhB was achieved by boron nitride nanosheets (BNNS)/polyvinyl alcohol (PVA) nanofiber membranes (Yin et al., 2019). In addition, a magnetic fibrous boron nitride nanocomposite (Fe_3O_4@*f*-BN) was synthesized for the SPE of 10 pesticides and exhibited great stability in 50 reuse cycles. (Y. Pang et al., 2018).

Recently our group has developed several approaches in construction, preparation and application of various functional *g*-BN-based nanomaterials, such as few-layered BN nanosheets prepared by the gas exfoliation process (Chao et al., 2019; Zhu et al., 2016; Zhu et al., 2017), gas-exfoliated porous monolayer BN, and *N*-terminated porous BN for desulfurization (Wu et al., 2017; Wu et al., 2018), Ag nanoparticle decorated BN and carbon-doped BN nanoplates for adsorption of dyes and antibiotic contaminants (Pang et al., 2017, 2018), *etc.* Different BN materials have been prepared and applied by other groups as well, such as BN short fibers for the adsorption of pollutant (Liu, Zhao, Luo, & Tang, 2019), highly porous BN for energy storage (Weng, Wang, Bando, & Golberg, 2014), and CuCo binary metal nanoparticles supported on BN nanofibers for catalytic hydrogenation (Yang et al., 2019), *etc*. The enhanced adsorption or catalytic performance of the developed materials could be confirmed by the enlarged surface area and functionalized surface structure. However, we found that there is an inevitable tendency for BN to aggregate in the aqueous phase caused by van der Waals interactions and self-induced π-π stacking, which restrict the application of BN (Chen et al., 2019; Fang, Jiang, Luo, & Geng, 2018). To address this problem, loading *g*-BN onto the surface of SiO_2 was attempted, as this strategy could significantly increase the hydrophilicity of BN and promote its dispersion in water. Moreover, the large surface area and abundance of SiO_2-associated active oxygen atoms (Xie et al., 2014) may induce a synergistic effect and further facilitate the adsorption capacity.

In the present work, few-layered graphene-like boron nitride (*g*-BN) was immobilized on dendritic SiO_2 nanospheres by a simple, and fast synthetic process. The as-prepared nano-composites, named as *g*-BN(x)@SiO_2 (x = wt% of BN), was applied as an efficient sorbent for SPE combining with HPLC for the extraction, pre-concentration, and determination of trace RhB and R6G. The adsorption performance was investigated by batches of equilibrium experiments. The factors that might affect the *g*-BN@SiO_2-based SPE performance for the extraction of RhB and R6G (sorbent dosage, extraction time, elution volume, cycle number, pH and ionic strength) were optimized. Applicability of the proposed methodology was investigated in chilli powder and beverage samples. We anticipated that this work will inspire to design more nano-adsorbents and apply for the preconcentration of pollutants in food samples.

2. Materials and methods

2.1. Materials

Cetyltrimethylammonium chloride (CTAC) and triethanolamine (TEA) were purchased from Sigma-Aldrich. Tetraethyl orthosilicate (TEOS) was purchased from Aladdin Reagent Co., Ltd. Urea ($CO(NH_2)_2$), while boric acid (H_3BO_3) and all other reagents were purchased from Sinopharm Chemical Reagent Co., Ltd (AR grade). All chemicals were used as received without purification. The chili powder and beverage of FARMER'S ORCHARD were purchased from the local supermarket.

2.2. Characterization

The FT-IR spectra were recorded on a Nicolet Nexus 470 Fourier transform infrared spectrometer (KBr, room temperature). The phase structural characteristics of the samples were determined by X-ray diffractometry (XRD) using a Bruker D8 diffractometer with Cu Kα radiation. The morphologies of the samples were determined by Hitachi H-700 Transmission Electron Micro-scope (TEM). In addition, N_2 adsorption–desorption isotherm was used for the calculation of the specific surface areas and porous property (BET).

2.3. Sample preparation

2.3.1. Synthesis of g-BN

Typically, boric acid and urea were dissolved in 40 mL of a methanol/water mixture in a molar ratio of 1:30. The solution was heated at 55 °C until the solvent was completely removed. A white solid was obtained, which was then transferred to a tube furnace and heated to 900 °C with a heating rate of 10 °C /min under N_2 atmosphere. After the temperature reached 900 °C, heating was continued for 5 h. Then the obtained powder was named as *g*-BN.

2.3.2. Synthesis of g-BN(x)@SiO_2

A CTAC solution (25%, wt%, 25 mL) and 0.18 mL of TEA were added to 36 mL of water and stirred gently at 60 °C for 30 min in a 100-mL round bottom flask. Then, 20 mL of TEOS a solution in 1-octadecene (20%) and a certain amount of *g*-BN were carefully added to the water–CTAC–TEA solution and kept at 60 °C in an oil bath upon stirring for 24 h. Finally, the collected products were dried in a vacuum oven at 80 °C for 12 h and calcined at 550 °C for 6 h to remove the template. The obtained powder was named *g*-BN(x)@SiO_2 where x was 0.5%, 1%, 5%, or 10%. The preparation of SiO_2 was the same but without the addition *g*-BN.

2.4. Adsorption capacity of g-BN(x)@SiO_2

Batches of static adsorption experiments were performed to investigate the adsorption behavior of RhB on *g*-BN(x)@SiO_2. Typically, 5 mg of *g*-BN(x)@SiO_2 was placed in a 25 mL RhB solution (200 mg/L) and shook in a thermostatic shaker at 130 rpm and 298 K for time *t* or till the sorption equilibrium was achieved. The concentration of the RhB residue at time *t* (C_t, mg/L) and in equilibrium (C_e, mg/L) was determined by ultraviolet–visible spectroscopy. The adsorption capacity at time *t* (q_t, mg/g) and in equilibrium (q_e, mg/g) was calculated using the equation $q_t = (C_0\text{-}C_t)m/V$, where *m* is the mass of the adsorbents and *V* is the volume of the RhB solutions. Sorption isotherms and thermodynamic studies were carried out with different initial RhB concentration (75–300 mg/L) at controlled temperatures of 298, 308, 318 and 328 K.

2.5. SPE procedure

Firstly, certain amounts of *g*-BN(1%)@SiO_2 were added to 50 mL of each sample solution, and the mixture was placed in an ultrasonic equipment for extraction of certain time. Then, the dyes-adsorbed *g*-BN (1%)@SiO_2 was separated from the solution by centrifugation and eluted for a few minutes with certain volume of methanol to desorb the pre-concentrated target analytes. Finally, the residue was filtered and injected into the HPLC system for the detection of the target analytes. To achieve high recovery for the target dyes, the *g*-BN(1%)@SiO_2 amount, the extraction time, the elution volume and time, cycle number, pH and ionic strength were optimized.

2.6. Food sample preparation

Chili powder (5 g) was accurately weighed, poured into a beaker,

and stirred (500 rpm) in 100 mL ethyl alcohol. After centrifugation, the obtained clear solution was evaporated to dryness at 45 °C under N_2 atmosphere. The residue was dissolved and diluted with methanol and stored in the dark for future analysis.

Accordingly, 50 mL of beverage and 50 mL of acetonitrile were poured into a beaker and stirred at 500 rpm. The next steps were same as above.

2.7. HPLC conditions

The HPLC separations were performed on a C18 reversed-phase column (250 mm × 4.6 mm I.D., 5 μm, Shimadzu Corporation, Japan) at 45 °C. The samples were injected through a 20 μL loop. The detection wavelength was at 545 nm, the mobile phase was methanol/water (5:5) containing 0.3% phosphoric acid, and the flow rate was 1 mL/min.

3. Results and discussion

3.1. Characterization of g-BN@SiO_2

The *g*-BN(x)@SiO_2 (x: wt% of BN) composites were characterized using XRD, FTIR spectroscopy, N_2 adsorption–desorption isotherms, and TEM.

Based on Fig. 1a, the *g*-BN(x)@SiO_2 exhibited a broad diffraction peak at around $2\theta = 23^{\circ}$, which was attributed to the amorphous nature of the SiO_2 support (Xun et al., 2016). However, no other characteristic peaks of *g*-BN were observed, indicating that *g*-BN was highly dispersed on the SiO_2.

The FTIR spectra of the *g*-BN(x)@SiO_2 samples are illustrated in Fig. 1b. The characteristic peaks of SiO_2 can be easily observed at 1090, 803, and 460 cm^{-1}, attributed to the stretching vibrations of Si–O–Si (*asym*) and Si–O–Si (*sym*) and the bending vibration of Si–O–Si, respectively (Xun et al., 2019; Zhang et al., 2017). Furthermore, the peaks at 1396 cm^{-1} and 805 cm^{-1}, were assigned to the in-plane B–N stretching vibration mode and B–N–B bending vibration mode of *g*-BN, respectively (Lu et al., 2018; Wang et al., 2018). Moreover, the peak intensity of 1396 cm^{-1} was enhanced by increasing the amount of the *g*-BN loading, while the characteristic peaks of SiO_2, and *g*-BN were superposed at 805 cm^{-1}.

N_2 adsorption–desorption isotherms of the composites are displayed in Fig. 1c. The SiO_2, *g*-BN(0.5%)@SiO_2, *g*-BN(1%)@SiO_2, and *g*-BN(5%)@SiO_2 samples exhibited typical type IV isotherms with a H2 hysteresis loop at $p/p_0 = 0.9$, while *g*-BN(10%)@SiO_2 showed type II isotherms. The observed changes may have been caused by the appearance of slit pores stacking by the *g*-BN nanosheets. Furthermore, the textural properties of the composites were affected by the *g*-BN loading (Table S1). The specific surface area and the pore size of *g*-BN@SiO_2 decreased by increasing the *g*-BN amount. However, *g*-BN(0.5%)@SiO_2 and *g*-BN(1%)@SiO_2 exhibited larger specific surface areas and pore volume/size than SiO_2, indicating that the proper amount of *g*-BN on SiO_2 promoted the specific surface areas.

The TEM images of *g*-BN(1%)@SiO_2, *g*-BN, and SiO_2 are presented in Fig. 2. *g*-BN exhibited a graphene-like thin-layered nanosheet structure (Fig. 2a), while pure SiO_2 possessed a highly uniform dendritic nanosphere structure with a mean particle size of ca. 107 nm (Fig. 2b). As shown in Fig. 2c, the *g*-BN nanosheets were anchored on the SiO_2 nanospheres, thus limiting the homogeneity of the nanospheres' size. The statistic diameter of *g*-BN(1%)@SiO_2 was 133 ± 23 nm (Fig. 2d).

3.2. Static adsorption capacity

The adsorption performance of *g*-BN(x)@SiO_2 (x = 0, 0.5%, 1%, 5%, and 10%) for the RhB dye was investigated in batch experiments, and the results are depicted in Fig. 3. Based on Fig. 3a, the adsorption rate of *g*-BN(x)@SiO_2 obviously increased as the adsorption capacity increased rapidly to 279–391 mg/g (88.7%–92.1% of the equilibrium value) within the first 10 min. After that time, the adsorption amount slowly increased and did not change significantly after 30 min. Furthermore, it was observed that *g*-BN(1%)@SiO_2 exhibited considerably higher adsorption capacity than SiO_2 and the other *g*-BN(x)@SiO_2 composites. The introduction of a proper *g*-BN amount into SiO_2 nanospheres thus facilitated the adsorption capacity to RhB. This synergistic effect may originate from the enhanced high dispersion of *g*-BN and the high surface area with abundant active sites in both *g*-BN and SiO_2. Moreover, the RhB amount adsorbed on *g*-BN(1%)@SiO_2 at equilibrium could reach 423 mg/g at the final equilibrium time (1 h), which was 29.8% higher than that of SiO_2.

The adsorption kinetics of RhB on *g*-BN(x)@SiO_2 were interpreted with pseudo-first- and pseudo-second-order order models to reveal the rate-determining step and the adsorption mechanism. The linear forms of the two kinetic models are presented in the Supporting Information (eq. S1 and S2), and the obtained relevant parameters of the adsorption kinetics are outlined in Table S2. The plots assuming pseudo-second-order kinetics presented the best linear relation, and their correlation coefficient (R^2) values were higher than 0.99 compared to those of the pseudo-first-order kinetics. Besides, the adsorption amounts obtained from experimental data (q_e,exp) were almost identical to those calculated from fitting results (q_e,*cal*) of the pseudo-second-order model. Therefore, the adsorption process of RhB on *g*-BN(x)@SiO_2 strictly fitted to the pseudo-second-order rate kinetic model. The ideal fit of this model implied that the adsorption rate was controlled by strong chemical interactions, such as electrostatic interaction, while the adsorption capacity was proportional to the number of active sites on the adsorbent (Jung, Lee, Choi, & Lee, 2019). $t_{1/2}$, which is the half-equilibrium time ($t_{1/2} = 1/(k_2 q_e)$), ranged from 2.13 to 3.59 min for all the *g*-BN(x)@SiO_2 composites (Table S2), indicating the fast rate nature of the adsorption process.

The adsorption isotherms of RhB on the *g*-BN(1%)@SiO_2 composite were analyzed by fitting the equilibrium adsorption data with the Langmuir and Freundlich isotherm models (eq. S3 and S4, respectively). The linear fitted plots of q_e *vs.* C_e for the two isotherm models are presented in Fig. 3b, and the isotherm parameters are listed in Table S3. According to the R^2 values and the average percentage error of APE% (eq. S5), the Langmuir isotherm model was more accurate for the

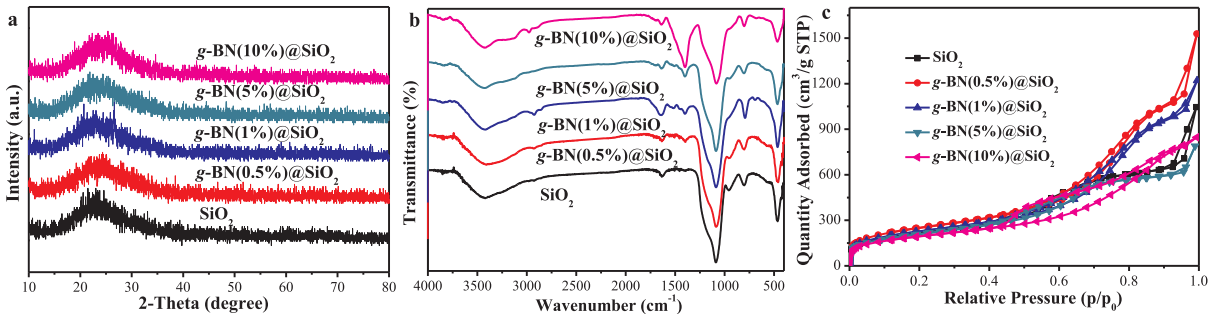

Fig. 1. (a) XRD patterns, (b) FTIR spectra, and (c) N_2 adsorption–desorption isotherms of *g*-BN(x)@SiO_2, where x = 0, 0.5%, 1%, 5%, and 10%.

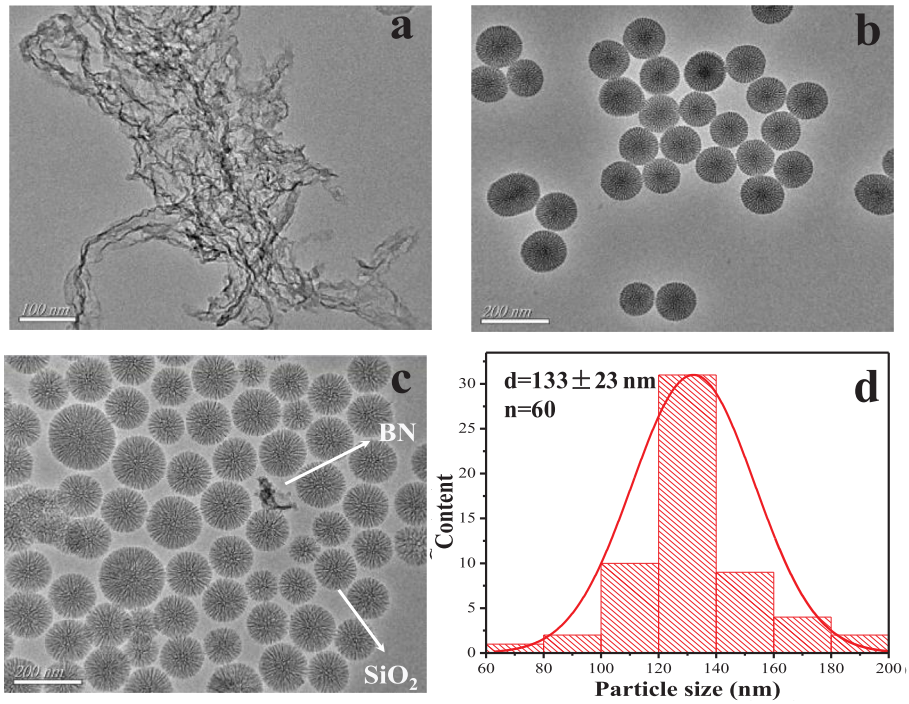

Fig. 2. TEM images of (a) *g*-BN, (b) SiO_2, and (c) *g*-BN(1%)@SiO_2. (d) Size distribution of *g*-BN(1%)@SiO_2.

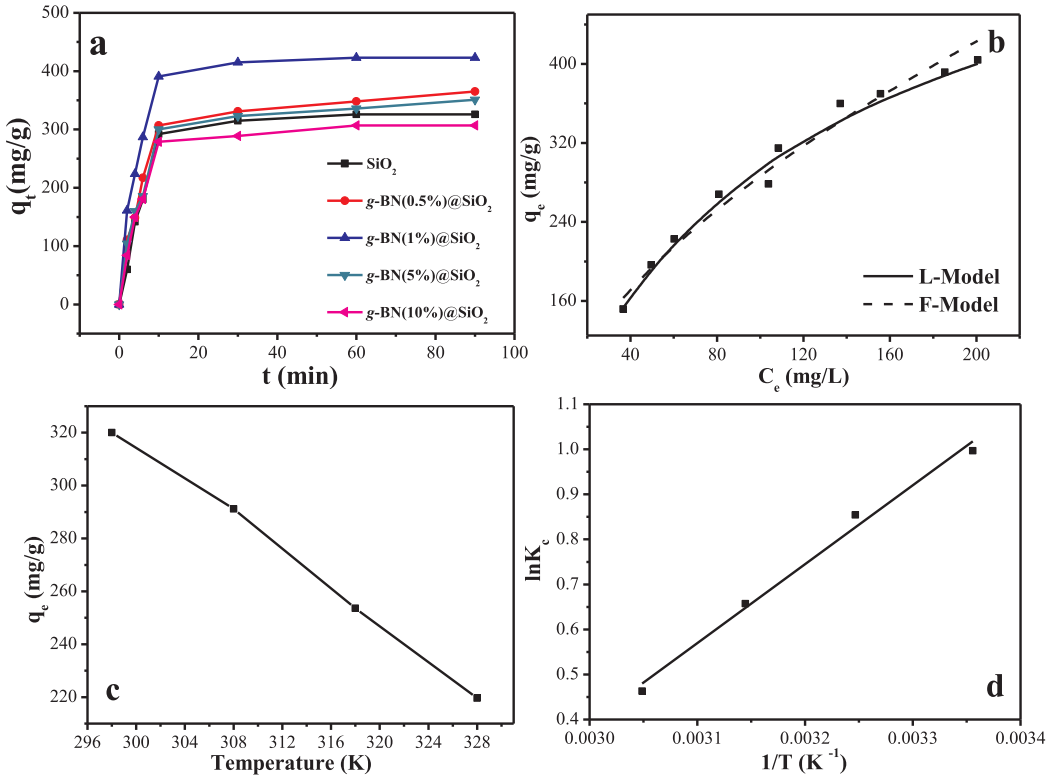

Fig. 3. (a) Effect of contact time on the adsorption capacity of RhB on *g*-BN(x)@SiO_2, where x = 0, 0.5%, 1%, 5%, or 10%. (b) Langmuir (L) and Freundlich (F) adsorption isotherm models to the experimental data for the adsorption of RhB on *g*-BN(1%)@SiO_2. (c) The effect of temperature on the adsorption of RhB on BN(1%)@SiO_2. (d) Van't Hoff regressions of the thermodynamic parameters.

equilibrium data than the Freundlich model, implying that the adsorption process can be attributed to the homogeneous binding sites on the *g*-BN(1%)@SiO_2 surface with monolayer coverage of RhB (Zhang, Wang, Wang, & Zhao, 2018). Favored by the enhanced surface area and the increased active sites of the composite, the maximum adsorption capacity (q_m) of *g*-BN(1%)@SiO_2 for RhB was 625 mg/g at 298 K.

The effect of the temperature on the adsorption was also investigated and the results are presented in Fig. 3c. The adsorption

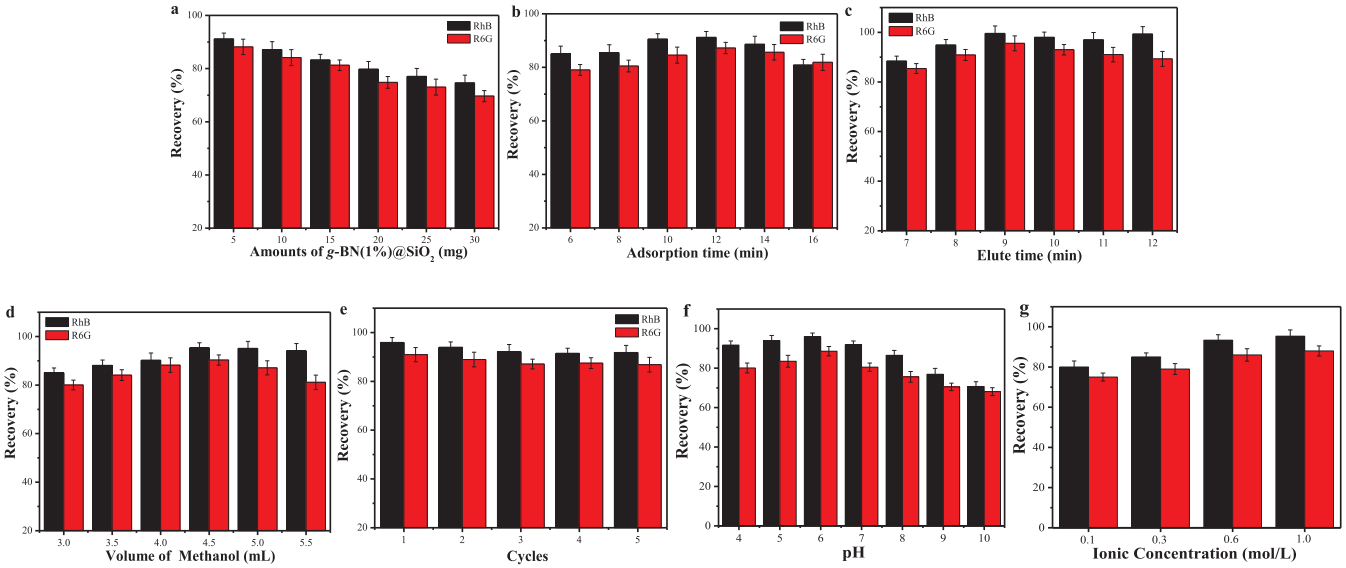

Fig. 4. Effect of (a) different amounts of *g*-BN(1%)@SiO_2, (b) extraction time, (c) elution volume, (d) elution time, (e) cycle number, (f) pH, and (g) ionic strength on the extraction recovery during the SPE procedure (black bar: RhB, red bar: R6G). (For interpretation of the references to color in this figure legend, the reader is referred to the web version of this article.)

capacity of RhB on *g*-BN(1%)@SiO_2 decreased with the temperature increase, implying an exothermic adsorption process. To further investigate the adsorption mechanism, the thermodynamic parameters of the Gibbs free energy change (ΔG, kJ/mol), the enthalpy change (ΔH, kJ/mol) and the entropy change (ΔS, kJ K^{-1} mol^{-1}) during the adsorption process were calculated by the equations S6–S8, and their values are listed in Table S4. The van't Hoff plots of ln*Kc vs.* $1/T$ are shown in Fig. 3d. All the ΔG values were negative, indicating that the capture of RhB by *g*-BN(1%)@SiO_2 occurs spontaneously. In addition, the negative ΔH value (−14.57 kJ/mol) suggested that the adsorption process was exothermic in nature, which was consistent with the tendency observed in Fig. 3c. Finally, the ΔS value was found to be −40.43 J K^{-1} mol^{-1}, suggesting that the solid/liquid interface tended to balance during the adsorption process.

3.3. Optimization of the SPE procedure

Factors, such as mass of adsorbents, extraction time, and elution time, solution volume, cycle number, pH, and ionic strength that influenced the extraction process, were also investigated (Fig. 4).

Fig. 4a illustrates the effect of the adsorbent amount on the extraction recovery of the RhB and R6G dyes. The increase in the *g*-BN(1%)@SiO_2 amount led to the gradual decrease of the dyes' recovery, indicating that the amount of dyes residues retained on the adsorbent increased as the mass of *g*-BN(1%)@SiO_2 increased under the same elution conditions. Among the examined quantities, 5 mg of *g*-BN(1%)@SiO_2 exhibited the optimum recovery and was used in the subsequent SPE procedure.

To evaluate the effect of the extraction time on the recovery of the dyes, extraction experiments with different extraction times ranging from 6 to 16 min were performed (Fig. 4b). During the first 12 min, the recovery of the dyes gradually increased, followed by a decrease as the extraction time further increased, indicating a dynamic process of the adsorption. It is also worth noting that the dyes would be desorbed from *g*-BN(1%)@SiO_2 if a long time of ultrasound was applied during the extraction process. Thus, 12 min were selected as the optimum extraction time.

Furthermore, a proper eluent is significant to reduce the interfering substances and improve the recovery. In this work, methyl alcohol was used as the eluent due to its excellent elution efficiency to dyes. The elution volume was also investigated at the range of 3.0–5.5 mL. As presented in Fig. 4c, the recovery was enhanced as the eluent volume increased to 4.5 mL, while it remained almost constant with a slight decrease as the volume further increased to 5.5 mL. Consequently, the optimum volume of methyl alcohol was 4.5 mL.

The effect of the elution time was also examined by varying the time from 7 to 12 min (Fig. 4d). The results indicated that the extraction recovery of the dyes increased with an elution time of up to 9 min but fluctuated as the time increased further. Thus, an elution time of 9 min was enough for the extraction. Consequently, the maximum recovery of RhB and R6G was improved to 96.6% and 90.3%, respectively, using the optimum SPE procedure that included 12 min of ultrasound extraction and 5 mg of *g*-BN(1%)@SiO_2, followed by dynamic elution for 9 min with 4.5 mL methanol.

Generally, the stability of an adsorbent is a key feature for its application. To estimate their reusability, the eluted *g*-BN(x)@SiO_2 composites were reused in the next cycle. Fig. 4e depicts the recovery percentage of the target after five reuse cycles. No obvious recovery loss was observed after five cycles, indicating the good stability of *g*-BN(x)@SiO_2 during the extraction process.

The effect of the pH value on the adsorption of RhB and R6G on *g*-BN(x)@SiO_2 was examined in a pH range of 4–10 using 50 mL of a 1.0 mg/L RhB and R6G solution, and the pH of the sample solution was adjusted with NaOH (0.1 M) or HCl (0.1 M). The pH value would affect the adsorption of dyes on *g*-BN(x)@SiO_2 by tuning their ionization (Fig. 4f). In the acidic solution, the dyes were positively charged and intermolecular forces and ionic interactions were the dominant interactions between dyes and *g*-BN(x)@SiO_2. The distinction between RhB and R6G may be their different pKa value (pK_{aRhB} = 3.2, pK_{aR6G} = 6.13). Instead, in the alkaline solution, dyes were negatively charged and the intermolecular forces were the main interactions. Moreover, the strength of the intermolecular forces was much weaker than that of the ionic interactions. Therefore, the recovery of RhB and R6G were greater in the acidic solution (Wu, Liu, Chen, & Yu, 2015).

The addition of a salt usually increases the ionic strength of the solution and would thus affect the recovery of RhB and R6G. As shown in Fig. 4g, the addition of NaCl in a concentration of up to 1 mol/L increased the recovery of dyes. Further increase of the NaCl concentration did not favor the dyes solubility, thus facilitating the diffusion of more dyes to the *g*-BN(x)@SiO_2 surface. Therefore, the hydrophobic effect may be the dominant feature of the extraction process (Chao et al., 2014).

Table 1
Retention time, linearity, R^2, LOD, and LOQ of the two dyes.

Target	Retention time (min)	Linear ranges (μg/L)	Linear equation[a]	R^2	*LOD* (μg/L)	*LOQ* (μg/L)
RhB	8.6	10–1000	y = 20920x − 43328	0.9998	2.8	9.2
R6G	11.9	10–1000	y = 161276x − 174268	0.9967	2.1	6.9

[a] y = peak area, x = initial concentration.

3.4. Analytical performance

Different standard solution concentrations of RhB and R6G dyes, ranging from 10 μg/L to 1000 μg/L, were prepared to obtain the calibration curves by plotting the peak area for each dye against its concentration. The calibration curve are $y = 20920x - 43328$ for RhB, $y = 161276x - 174268$ for R6G, where y is the peak area at 8.6, 11.9 min (retention time), respectively. x is the concentration of dyes. The limits of detection (*LOD*) (3 S/N, S: standard deviations of the obtained peak areas at the lowest concentration; N: slope of the working curve after extraction) and limits of quantification (*LOQ*) (10 S/N) are 2.8 μg/L and 9.2 μg/L for RhB and 2.1 μg/L and 6.9 μg/L for R6G, respectively. The obtained results are summarized in Table 1.

3.5. Real sample analysis

To demonstrate the feasibility and the reliability of the developed and optimized *g*-BN(1%)@SiO_2-based SPE/HPLC method, it was applied for the extraction, pre-concentration, and determination of RhB and R6G dyes in real food samples of chili powder and beverage. However, the dyes were not detected in real chili powder and beverage samples, indicating that their amount were lower than *LOQ*. Therefore, the samples were spiked with dyes in concentrations of 0.1 μg/mL, 0.5 μg/mL, and 10 μg/mL. As shown in Table 2, the spiked sample recovery of RhB and R6G ranged between 94.8% and 103.1%. The RSD % value, which reflects the repeatability of the method, was calculated for the 0.1 μg/mL, 0.5 μg/mL, and 10 μg/mL concentrations of the dyes. The values were less than 3.7% (n = 3), indicating the good precision for the analysis of food samples. Efficiency of the current method was compared with other SPE procedures. Based on the results shown in Table S5, the recoveries, and the *LOD*, *LOQ* and *RSD%* values of the proposed *g*-BN(1%)@SiO_2 based SPE/HPLC method were all better compared to other reported methods. Hence, the prepared *g*-BN(1%)@SiO_2 might serve as a promising SPE sorbent for the pre-concentration and analysis of RhB and R6G.

4. Conclusions

In this study, a novel nanocomposite, *g*-BN(x)@SiO_2, was fabricated and applied as a SPE adsorbent prior to HPLC-UV for the detection of illegal dye in foodstuffs. A synergistic effect with a significantly enhanced adsorption ability was observed, which originated from the highly dispersed active sites, and the enlarged surface area. The maximum monolayer adsorption capacity (q_m) of 625 mg/g was obtained for the RhB adsorption on *g*-BN(1%)@SiO_2 through a fast ($t_{1/2}$ = 2.13 min), exothermic, and spontaneous process. The maximum recovery of RhB and R6G was enhanced to 96.6% and 90.3%, respectively, under the optimum SPE conditions, namely, ultrasound extraction for 12 min using 5 mg of *g*-BN(1%)@SiO_2, followed by dynamic elution for 9 min with 4.5 mL methanol. Coupled with HPLC, satisfactory results including desirable repeatability, excellent linearity, and low *LOD* and *LOQ* values were achieved. An excellent spiked recovery of 94.8%–103.1% was also obtained using the developed method for analyzing RhB and R6G in real food matrices. Therefore, the *g*-BN(1%)@SiO_2-based material exhibits considerable potential as a promising adsorbent in SPE for the enrichment of illegal dyes and their detection in foodstuffs.

CRediT authorship contribution statement

Yanhong Chao: Investigation, Formal analysis, Writing - review & editing. **Jingyu Pang:** Investigation, Formal analysis, Writing - original draft. **Yan Bai:** Visualization, Supervision. **Peiwen Wu:** Validation. **Jing Luo:** Data curation. **Jing He:** Visualization. **Yan Jin:** Investigation, Data curation. **Xiaowei Li:** Formal analysis. **Jun Xiong:** Formal analysis. **Huaming Li:** Conceptualization, Resources. **Wenshuai Zhu:** Conceptualization, Methodology.

Declaration of Competing Interest

The authors declare that they have no known competing financial interests or personal relationships that could have appeared to influence the work reported in this paper.

Acknowledgement

Financial supports from the National Nature Science Foundation of China (Nos. 21878133, 21722604 and 21606113), Postdoctoral Science Foundation of China (No. 2019M652518), and Advanced Talents of Jiangsu University (No. 15JDG176). Major science and technology projects of Henan province (No. CX0001F01800), Major special project of Kaifeng (No. zd17005).

Table 2
Determination results of the real samples (n = 3).

Sample	Spiking level								
	0.1 μg/mL			0.5 μg/mL			10 μg/mL		
	C_{found} (μg/mL)	R (%)	RSD (%)	C_{found} (μg/mL)	R (%)	RSD (%)	C_{found} (μg/mL)	R (%)	RSD (%)
Chili powder									
RhB	0.0992	99.2	2.5	0.5155	103.1	1.8	9.98	99.8	1.6
R6G	0.0948	94.8	3.1	0.478	95.6	2.4	9.89	98.9	2.0
Beverage									
RhB	0.1011	101.1	3.0	0.4881	97.6	3.5	9.91	99.1	3.6
R6G	0.0958	95.8	3.3	0.4789	95.8	3.7	9.62	96.2	3.7

Appendix A. Supplementary data

Supplementary data to this article can be found online at https://doi.org/10.1016/j.foodchem.2020.126666.

References

Akkaya, E., Erulas, F. A., Buyukpinar, C., & Bakirdere, S. (2019). Accurate and sensitive determination of lead in black tea samples using cobalt magnetic particles based dispersive solid-phase microextraction prior to slotted quartz tube-flame atomic absorption spectrometry. *Food Chemistry, 297*, 124947. https://doi.org/10.1016/j.foodchem.2019.06.014.

Bagheri, A. R., Arabi, M., Ghaedi, M., Ostovan, A., Wang, X., Li, J., & Chen, L. (2019). Dummy molecularly imprinted polymers based on a green synthesis strategy for magnetic solid-phase extraction of acrylamide in food samples. *Talanta, 195*, 390–400. https://doi.org/10.1016/j.talanta.2018.11.065.

Chao, Y., Zhu, W., Wu, X., Hou, F., Xun, S., Wu, P., ... Li, H. (2014). Application of graphene-like layered molybdenum disulfide and its excellent adsorption behavior for doxycycline antibiotic. *Chemical Engineering Journal, 243*, 60–67. https://doi.org/10.1016/j.cej.2013.12.048.

Chen, J., Ma, Y., Wang, L., Han, W., Chai, Y., Wang, T., ... Ou, L. (2019). Preparation of chitosan/SiO2-loaded graphene composite beads for efficient removal of bilirubin. *Carbon, 143*, 352–361. https://doi.org/10.1016/j.carbon.2018.11.045.

Chen, J., & Zhu, X. (2016). Magnetic solid phase extraction using ionic liquid-coated core-shell magnetic nanoparticles followed by high-performance liquid chromatography for determination of Rhodamine B in food samples. *Food Chemistry, 200*, 10–15. https://doi.org/10.1016/j.foodchem.2016.01.002.

Dil, E. A., Ghaedi, M., Asfaram, A., Mehrabi, F., & Bazrafshan, A. A. (2018). Optimization of process parameters for determination of trace Hazardous dyes from industrial wastewaters based on nanostructures materials under ultrasound energy. *Ultrasonics Sonochemistry, 40*, 238–248. https://doi.org/10.1016/j.ultsonch.2017.07.022.

Fang, W., Jiang, X., Luo, H., & Geng, J. (2018). Synthesis of graphene/SiO2@polypyrrole nanocomposites and their application for Cr(VI) removal in aqueous solution. *Chemosphere, 197*, 594–602. https://doi.org/10.1016/j.chemosphere.2017.12.163.

He, G., Zhang, J., Hu, Y., Bai, Z., & Wei, C. (2019). Dual-template synthesis of mesoporous TiO2 nanotubes with structure-enhanced functional photocatalytic performance. *Applied Catalysis B: Environmental, 250*, 301–312. https://doi.org/10.1016/j.apcatb.2019.03.027.

Jung, K.-W., Lee, S. Y., Choi, J.-W., & Lee, Y. J. (2019). A facile one-pot hydrothermal synthesis of hydroxyapatite/biochar nanocomposites: Adsorption behavior and mechanisms for the removal of copper(II) from aqueous media. *Chemical Engineering Journal, 369*, 529–541. https://doi.org/10.1016/j.cej.2019.03.102.

Khani, R., Sobhani, S., & Yari, T. (2019). Magnetic dispersive micro solid-phase extraction of trace Rhodamine B using imino-pyridine immobilized on iron oxide as nanosorbent and optimization by Box-Behnken design. *Microchemical Journal, 146*, 471–478. https://doi.org/10.1016/j.microc.2019.01.038.

Li, F., Raza, A., Wang, Y. W., Xu, X. Q., & Chen, G. H. (2017). Optimization of surfactant-mediated, ultrasonic-assisted extraction of antioxidant polyphenols from rattan tea (Ampelopsis grossedentata) using response surface methodology. *Pharmacognosy Magazine, 13*(51), 446–453. https://doi.org/10.4103/pm.pm_159_16.

Liu, Z. W., Zhao, K., Luo, J., & Tang, Y. F. (2019). Highly efficient synthesis of hexagonal boron nitride short fibers with adsorption selectivity. *Ceramics International, 45*(17), 22394–22401. https://doi.org/10.1016/j.ceramint.2019.07.185.

Lu, L., He, J., Wu, P., Wu, Y., Chao, Y., Li, H., ... Zhu, W. (2018). Taming electronic properties of boron nitride nanosheets as metal-free catalysts for aerobic oxidative desulfurization of fuels. *Green Chemistry, 20*(19), 4453–4460. https://doi.org/10.1039/c8gc01625a.

Pang, J., Chao, Y., Chang, H., Li, H., Xiong, J., He, M., ... Zhu, W. (2017). Tuning electronic properties of boron nitride nanoplate via doping carbon for enhanced adsorptive performance. *Journal of Colloid and Interface Science, 508*, 121–128. https://doi.org/10.1016/j.jcis.2017.08.012.

Pang, J., Chao, Y., Chang, H., Li, H., Xiong, J., Zhang, Q., ... Li, H. (2018). Silver nanoparticle-decorated boron nitride with tunable electronic properties for enhancement of adsorption performance. *ACS Sustainable Chemistry & Engineering, 6*(4), 4948–4957. https://doi.org/10.1021/acssuschemeng.7b04481.

Chao, Y., Liu, M., Pang, J., Wu, P., Jin, Y., Li, X., ... Zhu, W. (2019). Gas-assisted exfoliation of boron nitride nanosheets enhancing adsorption performance. *Ceramics International*. https://doi.org/10.1016/j.ceramint.2019.06.117.

Pang, Y., Zang, X., Wang, M., Chang, Q., Zhang, S., Wang, C., & Wang, Z. (2018). Fibrous boron nitride nanocomposite for magnetic solid phase extraction of ten pesticides prior to the quantitation by gas chromatography. *Microchimica Acta, 185*(12), https://doi.org/10.1007/s00604-018-3103-0.

Qi, P., Liang, Z.-A., Wang, Y., Xiao, J., Liu, J., Liu, J., ... Zhang, X.-W. (2016). Mixed hemimicelles solid-phase extraction based on sodium dodecyl sulfate-coated nanomagnets for selective adsorption and enrichment of illegal cationic dyes in food matrices prior to high-performance liquid chromatography-diode array detection detection. *Journal of Chromatography A, 1437*, 25–36. https://doi.org/10.1016/j.chroma.2016.02.005.

Shen, T., Liu, S., Yan, W., & Wang, J. (2019). Highly efficient preparation of hexagonal boron nitride by direct microwave heating for dye removal. *Journal of Materials Science, 54*(12), 8852–8859. https://doi.org/10.1007/s10853-019-03514-8.

Song, Q., Liang, J., Fang, Y., Cao, C., Liu, Z., Li, L., ... Tang, C. (2019). Selective adsorption behavior/mechanism of antibiotic contaminants on novel boron nitride bundles. *Journal of Hazardous Materials, 364*, 654–662. https://doi.org/10.1016/j.jhazmat.2018.10.054.

Wang, C., Chen, Z., Yao, X., Chao, Y., Xun, S., Xiong, J., ... Li, H. (2018). Decavanadates anchored into micropores of graphene-like boron nitride: Efficient heterogeneous catalysts for aerobic oxidative desulfurization. *Fuel, 230*, 104–112. https://doi.org/10.1016/j.fuel.2018.04.153.

Wang, Q., Yao, L., Hao, L., Li, Y., Wang, C., Wu, Q., & Wang, Z. (2019). Ferrocene-based nanoporous organic polymer as solid-phase extraction sorbent for the extraction of chlorophenols from tap water, tea drink and peach juice samples. *Food Chemistry, 297*, 124962. https://doi.org/10.1016/j.foodchem.2019.124962.

Weng, Q., Wang, X., Bando, Y., & Golberg, D. (2014). One-step template-free synthesis of highly porous boron nitride microsponges for hydrogen storage. *Advanced Energy Materials, 4*(7), 1301525. https://doi.org/10.1002/aenm.201301525.

Wu, Z., Liu, Q., Chen, X., & Yu, J. (2015). Preconcentration and analysis of Rhodamine B in water and red wine samples by using magnesium hydroxide/carbon nanotube composites as a solid-phase extractant. *Journal of Separation Science, 38*(19), 3404–3411. https://doi.org/10.1002/jssc.201500246.

Wu, P., Yang, S., Zhu, W., Li, H., Chao, Y., Zhu, H., ... Dai, S. (2017). Tailoring N-Terminated Defective Edges of Porous Boron Nitride for Enhanced Aerobic Catalysis. *Small (Weinheim an der Bergstrasse, Germany), 13*(44), 1701857. https://doi.org/10.1002/smll.201701857.

Wu, P., Zhu, W., Chao, Y., Zhang, J., Zhang, P., Zhu, H., ... Dai, S. (2016). A template-free solvent-mediated synthesis of high surface area boron nitride nanosheets for aerobic oxidative desulfurization. *Chemical Communications, 52*(1), 144–147. https://doi.org/10.1039/c5cc07830j.

Wu, Y., Wu, P., Chao, Y., He, J., Li, H., Lu, L., ... Zhu, W. (2018). Gas-exfoliated porous monolayer boron nitride for enhanced aerobic oxidative desulfurization performance. *Nanotechnology, 29*(2), 025604. https://doi.org/10.1088/1361-6528/aa9bc7.

Xie, M., Xu, Y., Shen, H., Shen, S., Ge, Y., & Xie, J. (2014). Negative-charge-functionalized mesoporous silica nanoparticles as drug vehicles targeting hepatocellular carcinoma. *International Journal of Pharmaceutics, 474*(1–2), 223–231. https://doi.org/10.1016/j.ijpharm.2014.08.027.

Xun, S., Jiang, W., Guo, T., He, M., Ma, R., Zhang, M., ... Li, H. (2019). Magnetic mesoporous nanospheres supported phosphomolybdate-based ionic liquid for aerobic oxidative desulfurization of fuel. *Journal of Colloid and Interface Science, 534*, 239–247. https://doi.org/10.1016/j.jcis.2018.08.115.

Xun, S., Zhu, W., Chang, Y., Li, H., Zhang, M., Jiang, W., ... Li, H. (2016). Synthesis of supported $SiW_{12}O_{40}$-based ionic liquid catalyst induced solvent-free oxidative deep-desulfurization of fuels. *Chemical Engineering Journal, 288*, 608–617. https://doi.org/10.1016/j.cej.2015.12.005.

Yan, J. K., & Wang, Y. Y. (2015). Random-centroid optimization of ultrasound-assisted extraction of polysaccharides from cordyceps sinensis mycelium. *Current Topics in Nutraceutical Research, 13*(4), 167–171.

Yang, X., Li, Q. L., Li, L. L., Lin, J., Yang, X. J., Yu, C., ... Tang, C. C. (2019). CuCo binary metal nanoparticles supported on boron nitride nanofibers as highly efficient catalysts for hydrogen generation from hydrolysis of ammonia borane. *Journal of Power Sources, 431*, 135–143. https://doi.org/10.1016/j.jpowsour.2019.05.038.

Yin, C.-G., Ma, Y., Liu, Z.-J., Fan, J.-C., Shi, P.-H., Xu, Q.-J., & Min, Y.-L. (2019). Multifunctional boron nitride nanosheet/polymer composite nanofiber membranes. *Polymer, 162*, 100–107. https://doi.org/10.1016/j.polymer.2018.12.038.

Zhang, M., Wei, Y., Li, R., Zhu, W., Li, H., Zhang, Q., ... Li, H. (2017). Magnetic POM-based mesoporous silica for fast oxidation of aromatic sulfur compounds. *Fuel, 209*, 545–551. https://doi.org/10.1016/j.fuel.2017.08.001.

Zhang, Z., Wang, X., Wang, H., & Zhao, J. (2018). Removal of Pb(II) from aqueous solution using hydroxyapatite/calcium silicate hydrate (HAP/C-S-H) composite adsorbent prepared by a phosphate recovery process. *Chemical Engineering Journal, 344*, 53–61. https://doi.org/10.1016/j.cej.2018.03.066.

Zhu, W., Gao, X., Li, Q., Li, H., Chao, Y., Li, M., ... Dai, S. (2016). Controlled gas exfoliation of boron nitride into few-layered nanosheets. *Angewandte Chemie-International Edition, 55*(36), 10766–10770. https://doi.org/10.1002/anie.201605515.

Zhu, W., Wu, Z., Foo, G. S., Gao, X., Zhou, M., Liu, B., ... Zhu, H. (2017). Taming interfacial electronic properties of platinum nanoparticles on vacancy-abundant boron nitride nanosheets for enhanced catalysis. *Nature Communications, 8*, 15291. https://doi.org/10.1038/ncomms15291.

Zhuang, J., Zhang, J., Pang, J., Wang, A., Wang, X., & Zhu, W. (2019). Fabrication of pyrimidine/g-C_3N_4 nanocomposites for efficient photocatalytic activity under visible-light illumination. *Dyes and Pigments, 163*, 634–640. https://doi.org/10.1016/j.dyepig.2018.12.046.